Proceedings of the 20th National Conference on Superconductivity "New Phases, Concepts and Advances"

Brief Perspective of High-Temperature Superconductivity in the Cuprates: Strong Correlations Combined with Superexchange Match Experiment

J. Spałek*

Institute of Theoretical Physics, Jagiellonian University, Łojasiewicza 11, PL-30348 Kraków, Poland

Doi: 10.12693/APhysPolA.143.169 *e-mail: jozef.spalek@uj.edu.pl

High-temperature superconductivity encompasses the cuprates, nickelates, iron pnictides, and LaH_x compounds. The first three groups of compounds involve in the pairing electrons, which are strongly to moderately correlated, whereas in the last class of systems specific phonon excitations. In this overview, we concentrate first on the (semi)quantitative theory of high-T_C superconductivity in the cuprates based on our original vibrational approach beyond the renormalized mean-field theory. The model we mainly explore is the t–J–U model containing superexchange (kinetic exchange) combined with strong interelectronic correlations. Selected equilibrium and dynamic–excitation properties are analyzed briefly. General questions regarding the pseudogap and two-dimensional character of those systems are raised.

topics: high temperature superconductivity, strong electron correlations, cuprates, t–J–U model

1. Introduction

Originally, by high-temperature (high-T_C) superconductivity we understood that discovered 35 years ago in $La_{x-1}B_xTiO_y$, $La_{x-1}Sr_xCuO_y$, and $YBa_2Cu_3O_{7-\delta}$ systems. Later, the iron pnictide and chalogenide systems such as $LaFeAsO_{1-x}F_x$ and FeSe have been discovered. Recently, the nickelates $LaNiO_2$ and related compounds have been studied intensively. A separate class is formed by the LaH_{10+x}, for which the critical temperature has reached 250 K or even higher value, but for the latter case, an intensive debate concerning reproducibility of some results takes place. The principal difference between the hydrogen-rich and remaining systems is that in the case of LaH_{10+x}, the pairing of electrons seems to be caused by phonons, whereas in the cuprates, nickelates, and iron pnictides the strong to moderate interelectronic correlations play a decisive role. The aim of this brief overview is to compare our theoretical results for the cuprates with the principal experimental results in a consistent and quantitative way.

The structure of this brief review is as follows. In Sect. 2, we discuss the principal characteristics of the cuprates. In Sect. 3, we overview the qualitative features of our theory, whereas in Sect. 4, we provide explicit examples of a quantitative comparison of our results with experimental data. A brief outlook is deferred to Sect. 5. This paper aims to specify and summarize the most important results elaborated in a recent extensive topical review [1].

2. Principal characteristics of the cuprates

2.1. Structural and electronic specific features of the cuprates

The most striking structural property of the high-temperature superconducting cuprates and pnictides is their quasi-two-dimensionality, composed in the simplest situation of well-separated CuO_2 planes. This is the case for, e.g., $La_{1-\delta}Sr_\delta CuO_4$ or $Bi_2Sr_{1.6}La_{0.4}CuO_{6-\delta}$ mixed compounds. This simplifying assumption induced a series of studies of strictly two-dimensional models of high-T_C superconductivity, even though it is not exactly clear whether, strictly speaking, a spatially homogeneous two-dimensional transition to a superconducting state is possible at nonzero temperature ($T > 0$). The evidence for such an ordering is supported by the results for a single plane of FeSe [2].

The second most important feature is that the carriers in the CuO_2 plane are holes in the doped Mott insulator. The situation is schematically depicted in Fig. 1. Note that only Cu^{2+} ions are shown for the sake of clarity. Virtual hopping processes, also specified there, lead to the antiferromagnetic kinetic exchange representing the superexchange, whereas the real hopping processes provide the charge transport of single carriers and their pairing in both hole- and electron-doped case situations. Note a gradual character of transformation from an antiferromagnetic Mott insulator to a strongly correlated metal with doping. At this point, it is

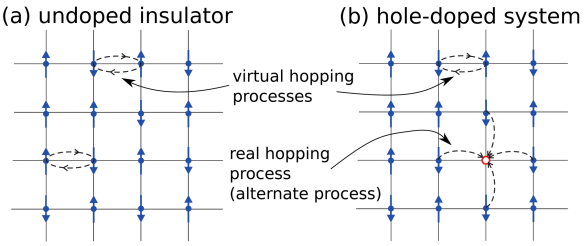

Fig. 1. Schematic representation of the particle dynamics in terms of hopping processes (dashed arrows) in the Mott-insulating state (a) and the strongly-correlated metal phase (b). Virtual hopping involves two consecutive back and forth direct hopping processes and occurs in both cases, (a) and (b). The direct hopping results in real motion of holes and occurs only in the strongly-correlated metal phase (b). In the strong-correlation regime, the direct hopping processes via doubly occupied configurations $|\uparrow\downarrow\rangle$ are precluded. In the last, case we speak about extremely strong correlations. The arrows surrounding the hole (red circle) mark possible real hoppings around it.

fair to say that, so far, it is not clear whether this changeover from the Mott insulator to the strongly correlated metal is a real quantum phase transition with an incipient quantum critical point, blurred by the substitutional disorder (e.g., Sr for La), taking place in La–Sr–O insulating planes, sandwiching the periodic arrangement of the CuO_2 planes, where the action takes place.

Another striking feature is the circumstance that the CuO_2 planes may be represented originally by the atomic $3d_{x^2-y^2}$ states, representing the highest positioned electron of nominally $3d^9$ shell of Cu^{2+} ion, hybridized with two $2p_x$ and $2p_y$ states of nominally O^{2-} ions. The situation is depicted schematically in Fig. 2a. This 3-orbital periodic structure, arranged into a square lattice, leads to the three bands specified in Fig. 2b; the $t_{\alpha\beta}$ parameters are the hopping integrals between the specified orbitals. The sign convention reflects the antibonding character of resulting p–d states.

Now, if the CuO_2 system is regarded as effectively a single-band system composed of $3d_{x^2-y^2}$ orbitals dressed with $2p_{x,y}$ orbitals, in which the latter states play only a passive role [3], then such a single-band Mott insulator is represented by a singly occupied set of Cu^{2+} ions. This situation, depicted in Fig. 1, where the $\uparrow$ and $\downarrow$ arrows specify the spins of the ninth electrons per site, may be regarded as the model of the Mott–Hubbard insulator. The doping $\delta \equiv 1 - n$ represents then the average number of hole carriers counted per site. If, however, one takes the three-orbital $3d_{x^2-y^2}$–$2p_{x,y}$ model, then the corresponding Mott–Hubbard insulator (called, in that case, the charge-transfer insulator) contains 5 electrons per $Cu^{2+}O_2^{2-}$ cluster (two $2p$ electrons per oxygen and one electron per copper). In that situation, the hole doping may be defined as $\delta \equiv 5 - n$, where n in both situations is the number of electrons per fundamental unit, Cu or CuO_2, respectively.

The fourth principal assumption is that the original microscopic parameters, such as the hoppings $t_{\alpha\beta}$ or interaction strength, do not vary essentially in the whole doping range where the superconductivity appears, i.e., for $0 \lesssim \delta \lesssim \frac{1}{3}$. Those bare parameters do vary from system to system, but mainly due to interelectronic correlations which induce their strong doping dependent renormalization. They complement the bare one-electron structure. Effectively, one should regard the single-band model description as that referring to the situation of the antibonding band (see Fig. 2b), containing effectively $1 - \delta$ electrons per copper. This point is to be verified later.

The final structural feature of the system is the experimental observation that the electronic properties in the normal state are those of practically two-dimensional metal, with the resistivity in plane/across plane $\rho_\parallel/\rho_\perp \sim 10^5$ in the optimal situation, and with metallic/semiconducting behavior of $\rho_\parallel/\rho_\perp$, respectively. The superconducting phase, on the contrary, is three-dimensional. This means that there is D = 2 to D = 3 dimensional changeover at the critical temperature. In other words, the interplanar coherence appears in the condensed state. This can be clearly shown when examining systematically single- versus multiplanar systems critical temperature T_C as a function of the number of closely spaced planes [4].

2.2. Theoretical models of strongly correlated square planar structure of the cuprates

In our group, we have concentrated on studying two theoretical models, namely the (extended) single-band Hubbard model under the acronym of t–U–J–V model (see Appendix) and the three-band $3d$–$2p_{x,y}$ model. In the latter situation, also its similarity to the one-band case under special circumstances has been explored [3]. The former represents the most general single-band model with short-range intersite interactions (and correlations), which reduces to either t–J or Hubbard model in proper limits. The three-band model, in turn, allows for an explicit discussion of the role of oxygen in particle dynamics and ordering, particularly in the metallic state. We overview each of them separately in the context of concrete results and compare them with the experiment.

3. The method and its qualitative interpretation

3.1. The method: Single-band model

The most general single-band model of correlated electrons has been discussed briefly in Appendix. In this section we limit ourselves to the so-called t–J–U–V model in the form [5]

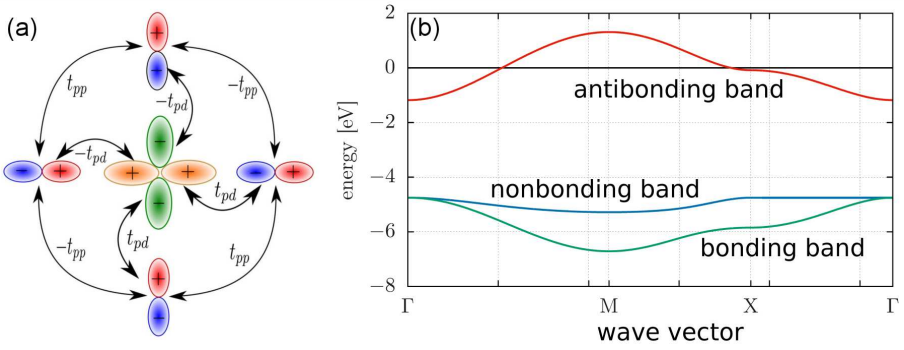

Fig. 2. Bare (without interaction) three-band structure in the tight binding approximation. (a) Definition of the hopping parameters between the p_x, p_y, and $d_{x^2-y^2}$ orbitals, with the sign convention for the antibonding orbital structure. This structural unit forms a basis of three-band model of the CuO_2 plane in the cuprates. (b) The band structure of the d–p model with microscopic parameters: $t_{pd} \simeq 1.13$ eV, $t_{pp} \simeq 0.49$ eV, and $\epsilon_{pd} \simeq 3.57$ eV. The Fermi energy is taken as the reference value and corresponds to the filling $n = 5$ per $Cu^{2+}O_2^{2-}$ complex, corresponding to half-filled antibonding band. This partially filled band is split off by about ϵ_{pd} from the remaining filled bands and reflects a single-hybridized (bare) band, the horizontal line marks the position of the Fermi energy for $n = 5$ electrons per CuO_2 unit [2]. In the strong correlation limit the antibonding band (and the other two) is split into two Hubbard subbands.

$$\hat{\mathcal{H}} = {\sum_{ij\sigma}}' t_{ij}\hat{a}^{\dagger}_{i\sigma}\hat{a}_{j\sigma} + U\sum_{i}\hat{n}_{i\uparrow}\hat{n}_{i\downarrow} + {\sum_{ij}}' J_{ij}\hat{\boldsymbol{S}}_i\hat{\boldsymbol{S}}_j + \frac{1}{2}{\sum_{ij}}'\left(V_{ij} - \frac{1}{2}J_{ij}\right)\hat{n}_i\hat{n}_j. \tag{1}$$

The parameters and consecutive terms are defined and explained in Appendix. The Hamiltonian (1) is used as a starting point for further analysis and solution for many-particle states. In our comprehensive review [1], we selected the approach based on a trial variational wave function and subsequently constructed a systematic diagrammatic expansion for the Gutzwiller-type wave function (DEGWF) which in the lowest order gives a renormalized mean-field theory (RMFT) in the form of statistically consistent Gutzwiller approximation (SGA) [6]. In general, the approach is based on a selection of the ground-state many-particle wave function $|\psi_G\rangle$ in the form

$$|\psi_G\rangle \equiv \hat{P}|\psi_0\rangle, \tag{2}$$

where $|\psi_0\rangle$ represents an uncorrelated (single-particle) state, to be defined later in the process of solving the model in a self-consistent manner. The nontrivial projection operator $\hat{P}$ is given by [7]

$$\hat{P} \equiv \prod_i \hat{P}_i = \prod_i \lambda_{i\Gamma}\ |\Gamma\rangle_{i\,i}\langle\Gamma| \tag{3}$$

with the wave function variational parameters $\lambda_{i,\Gamma} \in \{\lambda_{i,0}, \lambda_{i,\uparrow}, \lambda_{i,\downarrow}, \lambda_{i,\uparrow\downarrow}\}$, corresponding to the local (lattice site i) states $|\Phi\rangle$, $|\uparrow\rangle_i$, $|\downarrow\rangle_i$, and $|\uparrow\downarrow\rangle_i$, respectively. The consecutive states represent the empty, singly occupied states with spin quantum number $\uparrow$ and $\downarrow$, and doubly occupied states, all on the site i. For such a choice of the site representation, the $\lambda_{i,\Gamma}$ parameters weight the relative probability amplitudes of local occupancies appearance for each site. In the limit of large Coulomb repulsion ($U \gg W$, where W is the bare bandwidth) the double occupancies are absent. Additionally, we consider here translationally invariant paramagnetic state for which $\lambda_{i\uparrow} = \lambda_{i\downarrow} = \lambda_i$.

The ground state energy is determined by minimizing the variational expression for the ground state energy

$$E_G \equiv \langle\hat{\mathcal{H}}\rangle_G = \frac{\langle\,\Psi_G|\hat{\mathcal{H}}|\,\Psi_G\rangle}{\langle\,\Psi_G|\,\Psi_G\rangle} = \frac{\langle\,\Psi_0|\hat{P}\hat{\mathcal{H}}\hat{P}|\,\Psi_0\rangle}{\langle\,\Psi_0|\hat{P}^2|\,\Psi_0\rangle}. \tag{4}$$

It turns out that, by introducing the following additional ansatz for the $\hat{P}_i$ operator [7]

$$\hat{P}_i^2 \equiv 1 + x d_i^{HF}, \tag{5}$$

where x is yet another variational parameter, and by defining the quantities

$$\begin{aligned} d_i^{HF} &\equiv \hat{n}_{i\uparrow}^{HF}\hat{n}_{i\downarrow}^{HF}, \\ \hat{n}_{i\sigma}^{HF} &\equiv \hat{n}_{i\sigma} - \langle\hat{n}_{i\sigma}\rangle \equiv \hat{n}_{i\sigma} - n_0, \end{aligned} \tag{6}$$

with $n_0 \equiv \langle\psi_0|\hat{n}_{i\sigma}|\psi_0\rangle$, we can perform a systematic expansion of the functional (4) (for details see [1, 3]) and obtain explicitly the interesting physical properties in the correlated state which are determined through corresponding quantities in the uncorrelated state. Before detailed physical discussion, we should mention the method of defining the uncorrelated wave function ψ_0. Namely, in our approach, it is determined from another variational principle [8]

$$\frac{\delta}{\delta\langle\psi_0|}\Big[\mathcal{F} - \lambda\big(\langle\psi_0|\psi_0\rangle - 1\big)\Big] = 0, \tag{7}$$

where $\mathcal{F} \equiv \langle\hat{\mathcal{H}}\rangle_G$ expressed in terms of uncorrelated correlation functions. In effect, there are two intersite functions

$$P_{ij} \equiv \langle\hat{c}^{\dagger}_{i\sigma}\hat{c}_{j\sigma}\rangle, \quad \text{and} \quad S_{ij} \equiv \langle\hat{c}^{\dagger}_{i\uparrow}\hat{c}^{\dagger}_{j\downarrow}\rangle_0 \tag{8}$$

that represent averages of local hopping and pairing correlations in an uncorrelated state, respectively. The variational parameter λ is introduced to ensure that the wave function is normalized. The procedure of solving (7) is equivalent to Bogoliubov-type diagonalization of the effective Hamiltonian

$$\hat{\mathcal{H}}^{eff} \equiv \sum_{ij\sigma} t_{ij}\hat{a}^{\dagger}_{i\sigma}\hat{a}_{j\sigma} + \sum_{ij}\left(\Delta_{ij}\hat{a}^{\dagger}_{i\uparrow}\hat{a}^{\dagger}_{j\downarrow} + \Delta^{*}_{ji}\hat{a}_{i\downarrow}\hat{a}_{j\uparrow}\right), \tag{9}$$

where

$$t^{eff}_{ij} \equiv \frac{\delta\mathcal{F}}{\delta P_{ij}}, \tag{10}$$

and

$$\Delta^{eff}_{ij} \equiv \frac{\delta\mathcal{F}}{\delta S_{ij}}. \tag{11}$$

In effect, the determination of the uncorrelated properties reduces to the diagonalization of the Bardeen–Cooper–Schrieffer-type (BCS) Hamiltonian, and this in turn to the determination of the properties in the correlated state. As the averages in that state are factorized in terms of uncorrelated S_{ij} and P_{ij}, the latter procedure completes the determination of the wave function in the correlated state $|\psi_G\rangle$, provided that the remaining variational parameters are also determined [1, 3].

3.2. Three-band model: A brief perspective

As said above, strictly speaking, the elementary structural unit in two dimensions contains a single $3d_{x^2-y^2}$ orbital due to the ninth electron of Cu^{2+} ions and two $2p_x$ and $2p_y$ orbitals, each filled with two electrons in the parent (undoped) situation. Therefore, one has to formulate a three-band model to see at least, what is its connection to the widely used t–J–U–V single-band models, which should be regarded as a particular case of the present one. For that purpose, one starts from the Hamiltonian

$$\begin{aligned}\hat{\mathcal{H}} = &\sum_{ij]'\alpha\sigma} t^{pp}_{ij}\hat{p}^{\dagger}_{i\alpha\sigma}\hat{p}_{j\alpha\sigma} + \epsilon_{dp}\sum_{i\sigma}\hat{d}^{\dagger}_{i\sigma}\hat{d}_{i\sigma} \\ &+ {\sum_{ij\alpha\sigma}}' t^{pd}_{ij}(\hat{d}^{\dagger}_{i\sigma}\hat{p}_{i\alpha\sigma} + \text{h.c.}) \\ &+ U_d\sum_i \hat{n}_{di\uparrow}\hat{n}_{di\downarrow} + U_p\sum_i \hat{n}_{pi\alpha\uparrow}\hat{n}_{pi\alpha\downarrow}.\end{aligned} \tag{12}$$

In this version of the model the bare p–p hopping is assumed as nonzero only between nn–$2p$ electrons, where $t_{pp} \simeq 0.5$–1 eV, $t_{pd} \simeq 1.1$–1.3 eV is the single-particle hybridization between $3d$ and $2p$ states that induces an effective d–d hopping in the higher order for the relevant antibonding states, and $\epsilon_d - \epsilon_p \simeq 3.5$ eV — the so-called $p \to d$ charge transfer energy. The relevant intra-atomic p–p and d–d interactions have magnitudes $U_{pp} \simeq 4$–5 eV and $U_{dd} \simeq 8$–1 eV. The other interactions term such as, e.g., that $\sim U_{pd}$ are neglected, which is probably an oversimplified feature of our model.

The question is to what extent results of the one-band model represented by (1) and that starting from (12) are principally equivalent. A simple answer to this question is provided by inspection of the results in Fig. 2b and by noting that in the doped systems the interesting regime is then for $\delta \lesssim 1/3$. This, in effect, means that in the present version of the model, the holes are located in the antibonding band, since the p–d charge transfer gap $\epsilon_{pd} = \epsilon_d - \epsilon_p$ is quite large on the scale of all parameters except U_{dd}. This bare-band picture persists also upon inclusion of interaction as the neglected U_{pd} enlarges the charge transfer gap and U_{dd} does not reverse the trend, when $n_d \lesssim 1$. The variational procedure presented in Sect. 3.2 is more involved [3] so it will not be presented in this minireview. Perhaps, it is worth showing explicitly the comparison of the doping dependence of the d–d gap (see Fig. 2a) in the three-band model with that of the single band model (see Fig. 2b); the consecutive components $\Delta^{(i)}$ represent those between i-th neighbors (i-th coordination sphere). The component $\Delta^{(2)}$ is absent for the d-electrons, since the nearest neighbor d–d correlations are strongly antiferromagnetic, inducing the effective spin–triplet correlations between the second neighbors. This exclusion does not appear for d–p and p–p pairing components; but they are of rather minor importance [3]. The two figures in the panel illustrate to what extent two models (1- vs 3-bands) may be regarded as equivalent.

3.3. The main qualitative features of the approach

First of all, the two energy scales appear in a natural way, i.e., those described by $|\psi_G\rangle$ and $|\psi_0\rangle$, respectively, as exemplified by the physical gap Δ_G and the pseudogap Δ_{eff}. The question is whether those separate scales can be seen in the actual correlated state. To illustrate the two faces of the correlated fermionic liquid we have compared first the doping dependence of the so-called pseudogap and the superconducting gap, Δ_{eff} and Δ_{dd}, respectively. Those values have been compared with exemplary experimental results in Fig. 3a, b (see also [9]). The amplitude Δ_{eff} is obtained from the single-particle Hamiltonian (12), whereas $\Delta_{dd} \equiv \Delta_G$ is from solving the full expression $\langle\mathcal{H}\rangle_G$. Both gaps have the d-wave symmetry $\Delta_{G,eff}(\boldsymbol{k}) = \Delta_{G,eff}(\cos(k_x) - \cos(k_y))$. The SGA approach in one-band case leads only to a qualitative agreement with the data. The actual doping dependence of SGA gap in the Γ–X direction is shown in Fig. 4a, b for the two values of the hopping amplitude. We see that the agreement of our theory (SGA) with experiment is rather qualitative, as only the trend of the data is reproduced. However, we believe that inclusion of correlations (see Sect. 5) may improve the results exhibited in Fig. 4a essentially. Obviously, it is still to be carried out in the future (see also Fig. 3b).

As the second test of the two energy scales, we consider the single-electron dispersion relation obtained from the angle-resolved photoemission spectroscopy (ARPES) experiment. The exemplary comparison of our modified approach [10]

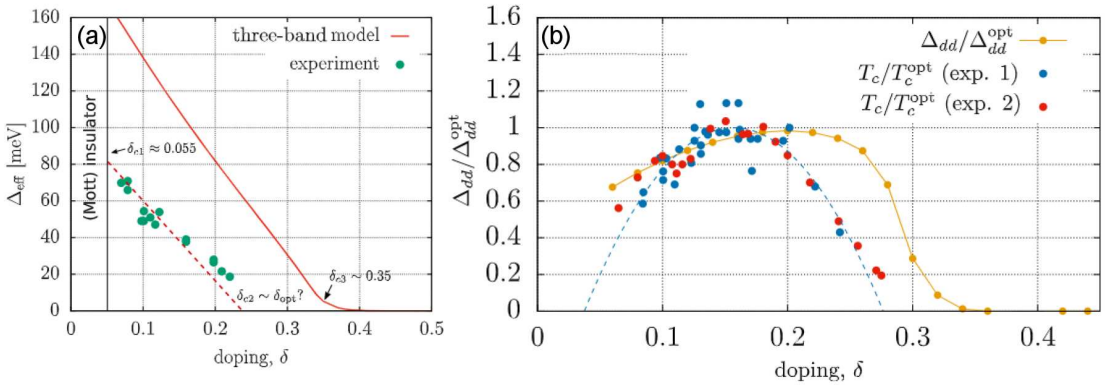

Fig. 3. (a) Plot of the experimentally observed pseudogap (points) as compared to theoretical results obtained from DE-GWF approach for the effective single-particle gap Δ_{eff} obtained within the three-band model. The Hamiltonian parameters are $U_d = 11$ eV, $U_p = 4.1$ eV, $\epsilon_{dp} = 3.2$ eV, $t_{pp} = 11$ eV. The critical doping levels and the Mott-insulator boundary are also marked. (b) Relative correlated d-wave gap component with intersite Coulomb interaction of magnitude $V_{dd} = 0.7$ eV. Experimental data sets 1 and 2 are taken from [2]. For a brief discussion of the role of quantum fluctuations in bringing the theoretical results to those obtained from experiment, see Sect. 6.

to experiment is shown in Fig. 5b (see also [11–13]). We see the comparison of the shift by Δk_0 of the linear dispersion relation for the correlated particles (the part below the kink) with respect to that close to the Fermi energy. Note that $\Delta k \equiv k - k_{\rm F}$ is the wave vector measured with respect to the Fermi surface point ($k = k_{\rm F}$) in the nodal direction. In Fig. 5b, we show the spectral two Fermi velocities $v_{\rm F,low}^{eff}$ and $v_{\rm F}^{corr}$, together with the renormalization factor $Z_{\rm nodal}$ in the latter case (see the corresponding dependence in Fig. 5c). Remaining labeling on those curves is self-explanatory [10]. Finally, in Fig. 5d the (weak) doping dependence of the Fermi wave vector is shown to agree with the experimental values.

The basic question to be asked is whether such a division into effective Landau quasiparticles and correlated particles of this quantum liquid (particles above and below the kink) is physically feasible. Our interpretation is that excitations at the Fermi level (in the nodal direction) can be regarded as true quasiparticles in the Landau sense, albeit renormalized differently, since our starting interaction comprises *a*ll relevant itinerant electrons and is short-range and strong in real space. On the contrary, the single-electron excitations from the region deeper below the Fermi level (with energy $\Delta\epsilon \equiv |\epsilon - \epsilon_F| \gtrsim 0.1$ eV) are dressed with the full interaction, in which the Hubbard term plays predominant role. Obviously, this division of a single quantum liquid of indistinguishable quantum particles into two parts is qualitative in nature and signals (by the kink's existence) a crossover behavior from a liquid of diluted quasiparticles to their truly correlated counterparts as one probes deeper into the Fermi sea. Such an interpretation requires further tests (see also further evidence in the next section). The division is coded in the selection of

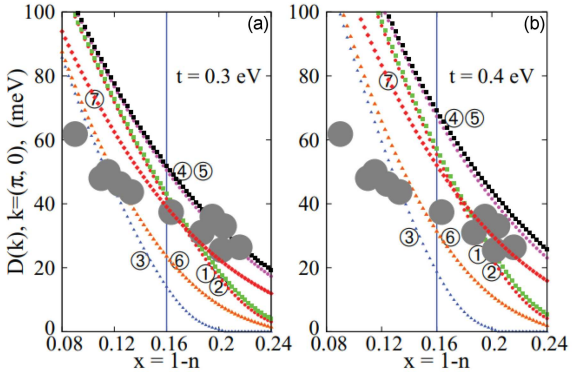

Fig. 4. Doping dependencies of the SC gap $\Delta_{eff}(\boldsymbol{k})$ at $\boldsymbol{k} = (\pi, 0)$ for different approximation schemes [6], curves 1–6, and for $t'/t = -0.27$ and $J/|t| = 0.3$. Large filled circles represent experimental data. Two values of t have been selected.

the wave function in the form (2), which contains a nonunitary projector $\hat{P}$, and is amplified by the fact that the starting (uncorrelated) wave function $|\psi_0\rangle$ also has nontrivial nature and is determined in a self-consistent manner that encompases also the states with broken symmetry from the start. We should note at the end that such a mixed Fermi–non-Fermi liquid properties have been also observed in the transport properties [14].

4. Detailed testing of the theory: Equilibrium properties

In this section we discuss selected detailed characteristic of high-temperature superconductors obtained within our real-space pairing among all itinerant electrons in our two-dimensional system.

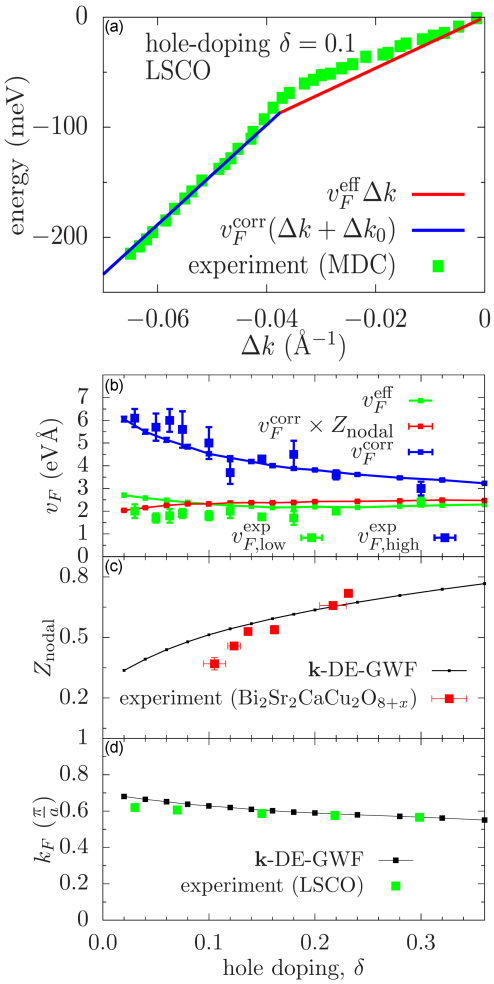

Fig. 5. (a) Experimental energy dispersion along the nodal direction for $La_{1.9}Sr_{0.1}CuO_4$ extracted from [11, 12]. The slopes of solid lines are obtained theoretically from the effective Hamiltonian (red) and first moment of the electron spectral function (red) for $\delta = 0.1$. (b) Doping-dependence of quasiparticle characteristic velocities above and below the kink (green and blue squares, respectively). Corresponding green and blue lines represent calculated effective- and correlated velocities calculated using $\boldsymbol{k}$-DE-GWF method. The red line is the correlated velocity multiplied by the calculated quasiparticle weight $Z_{\boldsymbol{k}}$. (c) Calculated $Z_{\boldsymbol{k}}$ as a function of doping (black points and lines), compared with experimental data for $Bi_2Sr_2CaCu_2O_{8+x}$ (red points, extracted from [13]). (d) Calculated Fermi wave vector along the nodal direction compared with data for $La_{2-x}Sr_xCuO_4$ for the same parameter values as those used in fitting curves in panels (a)–(c), see [10].

4.1. Inadequacy of the renormalized mean-field theory

Our work started with the analysis of the so-called renormalized mean-field theory (RMFT), which has been very popular in the first decade after the discovery of superconductivity in the nonstochiometric oxide $La_{2-x}Ba_xCuO_{4-\delta}$ and $YBa_2Cu_3O_{7-\delta}$. The approach was originally based on an improved version of the Gutzwiller approximation [15]. In our case, it takes the form of statistically consistent Gutzwiller approximation (SGA) [6]. In this approximation, the regime of doping, where the superconductivity exists is shown in Fig. 4a, b. The presence of antiferromagnetism at low doping can be reproduced qualitatively only after a careful selection of the carried out detailed SGA approximation scheme [16]. Furthermore, both the dependences of the (correlated) superconducting gap (see Fig. 4a) and particularly, of the dispersion relation of the single-particle excitations obtained from ARPES (see Fig. 5a, b) are not reproduced correctly. Explicitly, as we can see from the data included in Fig. 6b and on the basis of our later analysis based on the full DE-GWF (see Fig. 5), the Fermi velocity is rather flat, whereas the theoretical results shown in Fig. 6a, b exhibit the Fermi-liquid type of relative energy, diminishing steadily with decreasing doping. These results forced us to look for a theory, in which the SGA (or RMFT) results can be corrected in an essential way. In Sect. 4.2 we provide selected principal results illustrating the usefulness of our DE-GWF approach.

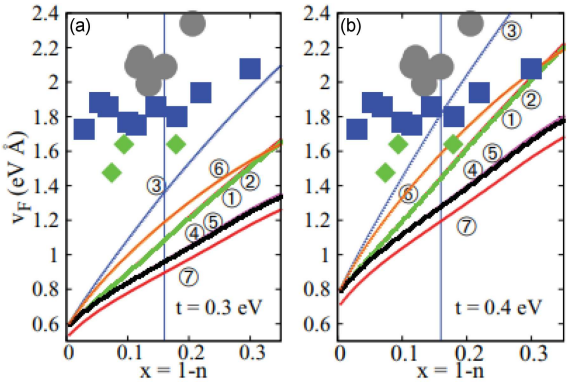

Fig. 6. Doping dependence of Fermi velocity in the nodal $[(0,0) \rightarrow (\pi,\pi)]$ direction. Experimental data (see [6]) are marked by diamonds for $YBa_2Cu_3O_{7-\delta}$ (YBCO), squares (LSCO), and solid circles (BSCCO). Two t values have been selected.

4.2. Additional results: Beyond mean-field theory and comparison with experiment

The most striking result to a theorist may be the fact, discovered experimentally some time ago [17], that the transition to the superconducting state, particularly in the regime of low doping, $\delta \lesssim 0.1$, takes place with the kinetic energy of the system getting lowered by the transition from the paramagnetic to superconducting phase. This is shown in Fig. 7a, where the results (squares with the error marked) have been plotted against the relative doping $\delta - \delta_{opt}$, where δ_{opt} is the optimal doping. Our theoretical curves require a more detailed explanation. Namely, the full curves represent our DE-GWF

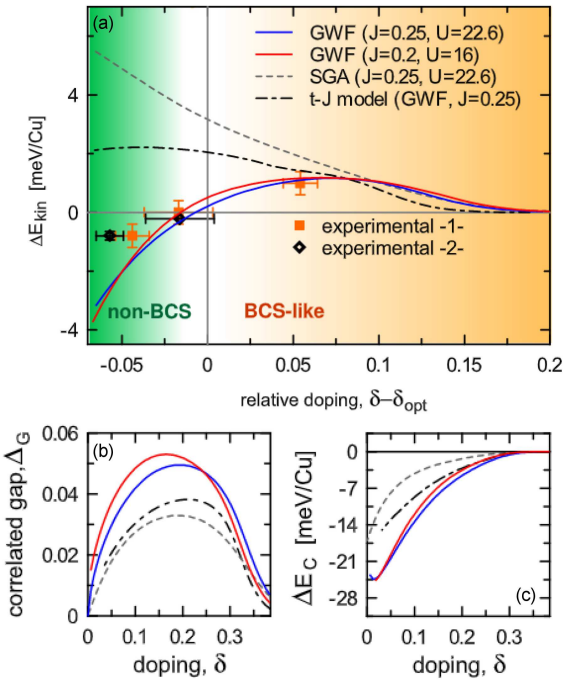

Fig. 7. Selected superconducting properties. (a) Kinetic energy gain ΔE_{kin} vs relative hole doping $\delta - \delta_{opt}$ (δ_{opt} is the optimal doping). The microscopic parameters are $J = 0.2|t|$, $U = 22.6|t|$ (for blue solid lines) and $J = 0.2|t|$, $U = 16|t|$ (for red solid lines); the experimental points are taken from [5]. For comparison, the results obtained with SGA method (gray dashed line) and those for the t–J model ($J = 0.25|t|$) in DE-GWF approximation (dash-dotted line) are also included. Note that only the t–J–U model solution describes the data in a quantitative manner. (b) Correlated-gap magnitude Δ_G and (c) the condensation energy $\Delta E_C = E_G^{SC} - E_G^{PM}$, both vs δ, are also shown for the respective values of microscopic parameters and models.

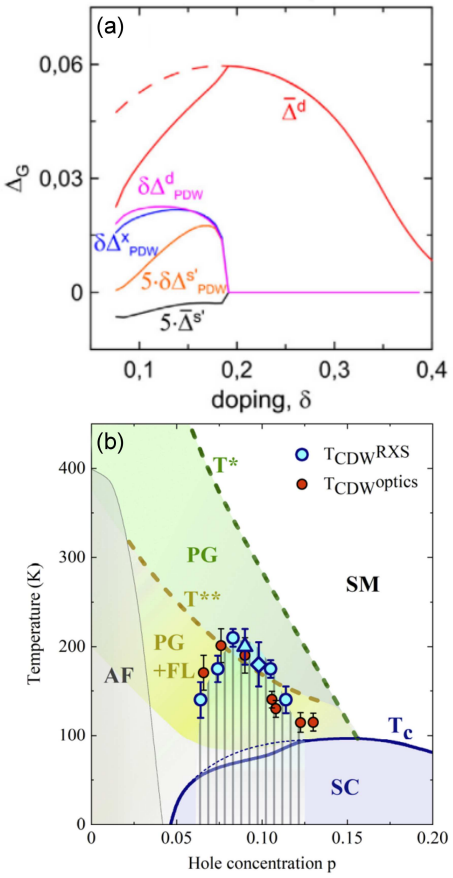

Fig. 8. The phase diagram comprising various charge-density-wave states: (a) theory and (b) experiment [3, 18–20]. For detailed discussion of various order-parameter components see [3]. Note that the onset of pair-density wave (PDW) induces also a small s-wave type of ordering in the system with the primary d-wave SC ordering. Pure d-wave superconducting phase appears only at and above the optimal doping, as observed.

solutions for two slightly different values of parameters within the t–J–U model [3]. The other two (dashed and dot-dashed) curves represent the SGA and the t–J model (beyond-SGA) solutions, respectively. None of the latter two solutions reproduces the singular behavior at low doping, at least for the type of detailed approach chosen. Parenthetically, the fact that only the t–J–U model, combined additionally with the DE-GWF, reflects the data in a quantitative manner, tells us that in order to reproduce them fully, one is forced to go beyond either the Hubbard or the t–J model. In such a situation, we interpret the simultaneous presence of both the Hubbard term with realistic values of $U \simeq 8$–10 eV and the kinetic exchange with its superexchange magnitude $J \simeq 0.1$ eV, as an implicit influence of the anionic $2p_{x,y}$ bands, not included in the standard one-band model, and producing the exchange interaction of desired magnitude, while keeping the Hubbard U in the realistic range at the same time.

In Fig. 7b and c we show the correlated gap magnitude of the d-wave solution and the condensation energy, respectively (the curve labelling and their meaning is the same as that in Fig. 7a). Note that $\Delta_G \simeq 0.03$–$0.05 = 15$ meV $\simeq 160$ K which is of the order of experimental value of T_C, but is substantially higher. This last fact is understandable as we do not account for thermodynamic and quantum fluctuations. Also, the condensation energy, i.e., the difference between the ground-state energies in normal and SC states is of the same magnitude and is strongly, but systematically, decreasing with increasing δ. Comparing Fig. 7a and Fig. 7c we see that surprising lowering with diminishing δ is related to the corresponding kinetic-energy decrease. Such difference in behavior may be the sign of the quantum spin–liquid effects, which are interrupted by the carrier localization. For detailed discussion of phase diagram and associated with it crossover from non-BCS to BCS-like see [3].

In the last decade, the presence of the charge-order presence has been intensely discussed, also in the context of the appearance of hidden charge density-wave quantum critical point at the optimal doping [17]. Leaving detailed discussion aside, we have analyzed the effect of finite-range correlations within our DE-GWF method [3] on the appearance of the charge-density-wave-type (CDW) state also with possible pair-density-wave (PDW) presence. We plotted in Fig. 8a the theoretical results and compared them with experimental data [3, 18–20]. Note the qualitative agreement between the two. In theory, the most remarkable is the charge-splitting analog to the Fulde–Ferrell state in the split electronic structure, which seems to reflect the experimental shape of the phase diagram. In passing, one can note the astonishing richness of phases for the two-dimensional structure of this model. The relation of those features to the persistence of the van Hove singularity in the correlated state should perhaps be discussed in more detail.

To illustrate further the relevance of our results, we have calculated, for the (approximately) same values of the microscopic parameters, the selected single-particle characteristics in the correlated state and within the three-band model [3]. They are quite similar to those obtained within the single-band model [9]. Explicitly, in Fig. 9 we display the doping dependence of the Fermi velocity (a), Fermi wave vector (b), and effective mass (c). What is surprising, is a rather weak δ dependence throughout the metallic phase. The dotted line represents our theoretical results, in the case (c) for two systems: La–Sr–Cu–O (LSCO) and Y–Ba–Cu–O (YBCO), respectively. Therefore, it is tempting to say that a nonmonotonic dependence of the critical temperature (T_C) or the correlated superconducting gap magnitude Δ_G is induced mainly by the competing character of the kinetic, exchange, and intraatomic Hubbard interactions. An analogical situation arises in the systems near the Mott–Hubbard insulator–metal transition [21].

At the end, one should note that a discussion of the onset on nemacity appears also in the systems, and was discussed within DE-GWF [22]. All in all, these results demonstrate the usefulness and effectiveness of the DE-GWF method, which represents a systematic approach beyond the mean-field type approach for these strong correlated systems. The whole approach bases on finite but large U ($U \gtrsim W$) combined with strong superexchange interactions.

5. Extension: Paramagnons and plasmons dynamic excitations

So far, the whole DE-GWF analysis was based on taking into account the static intersite correlations of increased range [1], starting from SGA. We have extended this analysis to collective dynamic excitations (paramagnons and plasmons) by

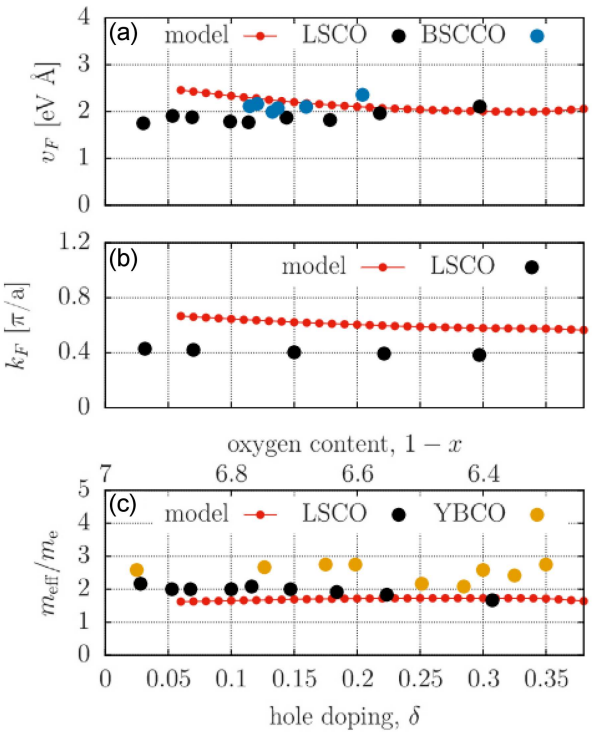

Fig. 9. The basic characteristics calculated for the three-band model. (a) Fermi velocity $v_{\rm F}$, (b) Fermi wave-vector $k_{\rm F}$, and (c) effective mass enhancement m_{eff}/m_e as a function of hole doping δ. The parameters are: $t_{pd} = 1$ eV, $t_{pp} = 0.4$ eV, $\epsilon_{pd} = 3.2$ eV, $U_d = 11$ eV, and $U_p = 4.1$ eV. Note a quite smooth δ dependence of all the single-electron parameters.

starting again from SGA and including long-range quantum fluctuations in the lowest order within $1/N$ expansion [22–25]. Here, we summarize briefly only the results for spin fluctuations spectrum in the Gaussian approximation. The results are summarized in the panels composing Fig. 10. The theoretical results are marked by the color scale (on the right side of the panels) and by the broken curves in Fig. 10a–c. The curves in Fig. 10f and g compare the theoretical results explicitly with experiment, as well as show the differences for the doping $\delta = 1-n = 0.12$ between those obtained in random phase-approximation (RPA) and those obtained in SGA (i.e., without correlations included). Only the full theory SGA+1/N compares excellently with experiment. A similar theory can be formulated for the plasmon excitations [22–25] (see also the relevant contribution to this volume [26]). One should mention that in describing the exhibited paramagnon-excitation characteristics, a standard damped oscillator representation of the theoretical results was involved. This approximate (Lorentzian) representation of the excitation spectrum should be considered carefully, and perhaps, a more general approach is required. We should see a progress along this line in the near future.

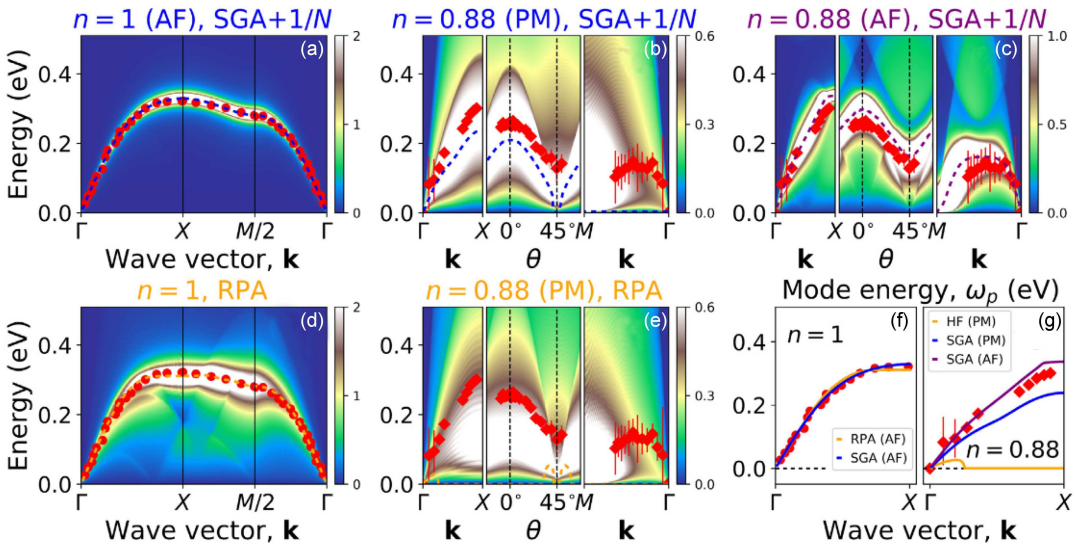

Fig. 10. Imaginary parts of transverse dynamical spin susceptibility for obtained within one-orbital Hubbard model with nearest- and next-nearest-neighbor hopping integrals included, and comparison with experiment for $La_{2-\delta}Sr_{\delta}CuO_4$ (LSCO). The model parameters are $t = -0.34$ eV, $U = 7|t|$. Panels (a) and (b) represent magnetic response at half filling ($n = 1$) in the antiferromagnetic state, obtained within $SGA_x{+}1/\mathcal{N}_f$ and RPA, respectively. The spectra are similar and both of them match neutron scattering data for LSCO (red circles). The dashed lines are the paramagnon energies obtained from theoretical intensities using damped harmonic oscillator model. Panels (c) and (d) result from the same analysis, but for hole-doped system ($n = 0.88$) in the paramagnetic state. Here, the differences are qualitative, i.e., the $SGA_x + 1/\mathcal{N}_f$ method yields propagating magnetic excitations along Γ–M line, whereas within RPA one obtains overdamped dynamics (see dashed curves and was discussion in the text). The agreement of the SGA+$1/N$ with RIXS data (diamonds) is semi-quantitative. Panel (e) shows $SGA_x + 1/\mathcal{N}_f$ results in the antiferromagnetic phase at lower temperature. In (f)–(g) we compare the theoretical RPA and $SGA_x + 1/\mathcal{N}_f$ paramagnon dispersion with experiment, see [22].

6. Conclusions

We have overviewed here selected basic characteristics of high-temperature superconducting cuprates. This paper summarizes some of the main results elaborated in detail in a comprehensive review [1]. The principal results and their favorable (semi)quantitative comparison with experiment support the fundamental concept of strong correlations combined with superexchange (kinetic exchange in one-band version of the theory) as the mechanism of the spin–singlet d-wave pairing in the cuprates. As we showed in [1] and also here, it is indispensable to formulate the theory beyond any version of the (renormalized) mean-field theory. What is still lacking is the incorporation of the quantum spin and charge fluctuations in the single-particle description of the normal-state properties to reproduce (or correct) the properties such as the linear electrical resistivity or pseudogap presence, to obtain a more complete quantitative picture. We should be able to see a progress along these lines in the near future. Also, the form of a single-band starting Hamiltonian relation to its more general three-band formulation, with an explicit inclusion of the superexchange in the metallic phase, should be reanalyzed carefully. Finally, the role of the third dimension is still to be incorporated into our theory to see explicitly the correction (if any) of the apical (interplane) oxygen may have in the formation of the $3d$ superconducting state.

Parenthetically, this article concludes the series of the minireviews published in the present journal over the years [27, 28].

Acknowledgments

The work reported in this paper was financially supported by the grants OPUS Nos. UMO–2018/29/B/ST3/02646 and UMO–2021/41/B/ST3/04070. The cooperation and multiple discussions of the results with Drs. Maciej Fidrysiak, Michał Zegrodnik, and Andrzej Biborski have been the most important factor in making this project so fruitful. I thank also to my Ph.D. student Maciek Hendzel for technical help during the writing of this report.

Appendix: From classical Coulomb repulsion to extended Hubbard model

The classical repulsive Coulomb interaction between two charges is long-range, changing with their mutual distance $|\boldsymbol{r}_i - \boldsymbol{r}_j|$ as

$$V_{12} \equiv V(\boldsymbol{r}_i - \boldsymbol{r}_j) = \frac{1}{\kappa}\frac{q_1 q_2}{|\boldsymbol{r}_i - \boldsymbol{r}_j|}. \tag{13}$$

For continuous charge densities $n(\boldsymbol{r}_i)$ and $n(\boldsymbol{r}_j)$, it takes the static Lenard–Wiechert form

$$V_{12} = \frac{e^2}{\kappa} \int \mathrm{d}^3\boldsymbol{r}\, \mathrm{d}^3\boldsymbol{r}' \, \frac{n(\boldsymbol{r}) n(\boldsymbol{r}')}{|\boldsymbol{r}-\boldsymbol{r}'|}. \tag{14}$$

For $n_i(\boldsymbol{r}) = \delta(\boldsymbol{r}-\boldsymbol{r}_i)$, (14) reduces to (13). In turn, in wave mechanics, the interaction between two charges is

$$V_{12} = \frac{e^2}{\kappa} \int \mathrm{d}^3\boldsymbol{r}\, \mathrm{d}^3\boldsymbol{r}' \, \frac{|\phi_1(\boldsymbol{r})|^2 |\phi_2(\boldsymbol{r}')|^2}{|\boldsymbol{r}-\boldsymbol{r}'|}, \tag{15}$$

where now $|\phi_i(\boldsymbol{r})|^2$ is the probability density for the i-th particle. Finally, in quantum field theory, the static interaction for indistinguishable particles is of the following operator form

$$\hat{V} = \frac{1}{2} \sum_{ijkl} \sum_{\sigma\sigma'} V_{ijkl}\, \hat{a}^\dagger_{i\sigma} \hat{a}^\dagger_{j\sigma'} \hat{a}_{l\sigma'} \hat{a}_{k\sigma}, \tag{16}$$

with

$$V_{ijkl} = \int \mathrm{d}^3\boldsymbol{r}\, \mathrm{d}^3\boldsymbol{r}' \, \phi^*_{i\sigma}(\boldsymbol{r}) \phi^*_j(\boldsymbol{r}') \frac{e^2}{\kappa|\boldsymbol{r}-\boldsymbol{r}'|} \phi_k(\boldsymbol{r}) \phi_l(\boldsymbol{r}'). \tag{17}$$

The indices (i,j,k,l) run over all possible single-particle states $\phi_{i\sigma}(\boldsymbol{r})_{i=1,2,\ldots,N}$, and (σ,σ') are spin quantum numbers for particular fermions characterized by (i,j,k,l). We see that in (17), the probability densities $|\phi_i(\boldsymbol{r})|^2$ and $|\phi_j(\boldsymbol{r}')|^2$ are replaced by quantities $\phi^*_i(\boldsymbol{r})\phi_j(\boldsymbol{r}')$ and $\phi_k(\boldsymbol{r})\phi_l(\boldsymbol{r}')$, respectively. We may say that they express roughly overlap functions, but strictly speaking, the states $\phi_i(\boldsymbol{r})$ and $\phi_j(\boldsymbol{r})$ are usually orthogonal, i.e., $\int \mathrm{d}^3\boldsymbol{r} \phi^*_i(\boldsymbol{r})\, \phi^*_j(\boldsymbol{r}) = \delta_{ij}$.

The question we are interested in is what happens if the wave functions $\phi_i(\boldsymbol{r})$ are close to their atomic counterparts. In that limit, (i,j,k,l), when selected as the parent atomic-state site positions, are far enough from each other that the largest contribution to (17) comes from the term $i=j=k=l$, i.e.,

$$V_{iiii} = \frac{e^2}{k} \int \mathrm{d}^3\boldsymbol{r}\, \mathrm{d}^3\boldsymbol{r}' \, \frac{|\phi_i(\boldsymbol{r})|^2 |\phi_i(\boldsymbol{r}')|^2}{|\boldsymbol{r}-\boldsymbol{r}'|}. \tag{18}$$

We call this term a director Coulomb interaction term and this form of potential effectively has (15) (also (14)). Now, (16) in the second quantization reduces to the Hubbard interaction term if we take only (18) out of all the terms appearing in (17). Hence,

$$\hat{V}^{(1)} \equiv \frac{1}{2} \sum_{i\sigma} V_{iiii}\, \hat{n}_{i\sigma} \hat{n}_{i\bar{\sigma}} \equiv U \sum_i \hat{n}_{i\uparrow} \hat{n}_{i\downarrow}. \tag{19}$$

In other words, this term predominates over all remaining terms if the overlap functions $\phi^*_i(\boldsymbol{r})\phi_j(\boldsymbol{r}')$ are the only relevant quantities for $i=j$, so the neighboring atomic states $\phi_i(\boldsymbol{r})$ and $\phi_j(\boldsymbol{r})$ are well separated. This assumption is the fundamental concept validating Hubbard's model, which represents a particular limit of (16), namely

$$\hat{\mathcal{H}} = \sum_{ij\sigma} t_{ij}\, \hat{a}^\dagger_{i\sigma} \hat{a}_{j\sigma} + U \sum_i \hat{n}_{i\uparrow} \hat{n}_{i\downarrow}. \tag{20}$$

This (still unsolved) model applies to many physical systems, albeit often only semiquantitatively.

In the present analysis, the nearest-neighbor Coulomb interactions are also important. Then, we are dealing with two-state (two-site) terms, namely

$$\begin{aligned} \hat{V}^{(2)} = {} & \frac{1}{2}{\sum_{ij}}' K_{ij} \hat{n}_i \hat{n}_j - \frac{1}{2}{\sum_{ij}}' J^H_{ij} \left(\hat{\boldsymbol{S}}_i \hat{\boldsymbol{S}}_j - \frac{1}{4} \hat{n}_i \hat{n}_j \right) \\ & + \frac{1}{2}{\sum_{ij\sigma}}' V_{ij}{}' (\hat{n}_{i\sigma} + \hat{n}_{j\sigma}) (\hat{a}^\dagger_{i\bar{\sigma}} \hat{a}_{j\bar{\sigma}} + \hat{a}^\dagger_{j\bar{\sigma}} \hat{a}_{i\bar{\sigma}}) \\ & + {\sum_{ij}}' J'_{ij} (\hat{a}^\dagger_{i\uparrow} \hat{a}^\dagger_{i\downarrow} \hat{a}_{j\downarrow} \hat{a}_{j\uparrow} + \text{h.c.}), \end{aligned} \tag{21}$$

where the first term is the direct Coulomb intersite term, the second represents the direct (Heisenberg) exchange interaction, the third is the so-called correlated hopping, and the last term is the pair hopping term (for details see [1]). The first two terms, when added to (20), give the extended Hubbard model. Note that the exchange term (second term) contains also the effective kinetic exchange interaction, hence, J_{ij} becomes negative. In effect, by redefining the constants $J_{ij} \equiv J^H_{ij} - J^{\mathrm{kex}}$ (where "kex" labels kinetic exchange contribution), $V_{ij} = \frac{1}{2} K_{ij} + \frac{1}{4} J_{ij}$, we obtain the t–U–J–V model in the form

$$\begin{aligned} \hat{\mathcal{H}} = {} & {\sum_{i\sigma}}' t_{ij} \hat{a}^\dagger_{i\sigma} \hat{a}_{i\sigma} + U \sum_i \hat{n}_{i\uparrow} \hat{n}_{i\downarrow} \\ & + {\sum_{ij}}' J_{ij} \hat{\mathbf{S}}_i \hat{\mathbf{S}}_j + \frac{1}{2}{\sum_{ij}}' V_{ij} \hat{n}_i \hat{n}_j. \end{aligned} \tag{22}$$

The results obtained with this model and its particular versions are discussed in detail in the main text.

References

[1] J. Spałek, M. Fidrysiak, M. Zegrodnik, A. Biborski, *Phys. Rep.* **959**, 1 (2022).

[2] Z. Wang, C. Liu, Y. Liu, J. Wang, *J. Phys. Condens. Matter* **29**, 253001 (2017).

[3] M. Zegrodnik, A. Biborski, M. Fidrysiak, J. Spałek, *Phys. Rev. B* **99**, 104511 (2019).

[4] K. Byczuk J. Spałek, *Phys. Rev. B* **53**, R518 (1996).

[5] M. Zegrodnik, J. Spałek, *Phys. Rev. B* **95**, 024507 (2017).

[6] J. Jedrak, J. Spałek, *Phys. Rev. B* **83**, 104512 (2011).

[7] J. Bünemann, T. Schickling, F. Gebhard, *Europhys. Lett.* **98**, 27006 (2012).

[8] J. Kaczmarczyk, *Philos. Mag.* **95**, 563 (2015).

[9] S. Hüfner, M.A. Hossain, A. Damascelli, G.A. Sawatzky, *Rep. Prog. Phys.* **71**, 062501 (2008).

[10] M. Fidrysiak, M. Zegrodnik, J. Spałek, *J. Phys. Condens. Matter* **30**, 475602 (2018).

[11] X.J. Zhou, T. Yoshida, A. Lanzara et al., *Nature* **423**, 398 (2003).

[12] K. Matsuyama, E. Perepelitsky, B.S. Shastry, *Phys. Rev. B* **95**, 165435 (2017).

[13] M. Hashimoto, T. Yoshida, H. Yagi et al., *Phys. Rev. B* **77**, 094516 (2008).

[14] N. Barisić, M.K. Chan, Y. Li, G. Yu, X. Zhao, M. Dressel, A. Smontara, M. Greven, *Proc. Natl. Acad. Sci.* **110**, 12235 (2013).

[15] P.W. Anderson, P.A. Lee, M. Randeria, T.M. Rice, N. Trivedi, F.C. Zhang, *J. Phys. Condens. Matter* **16**, R755 (2004).

[16] M. Abram, M. Zegrodnik, J. Spałek, *J. Phys. Condens. Matter* **29**, 365602 (2017).

[17] G. Deutscher, A.F. Santander-Syro, N. Bontemps, *Phys. Rev. B* **72**, 092504 (2005).

[18] C. Di Castro, *Condens. Matter* **5**, 70 (2020).

[19] I. Biało, Ph.D. Thesis, AGH University of Science and Technology, and TU Wien, 2020 (unpublished).

[20] W. Tabiś, B. Yu, I. Bialo et al., *Phys. Rev. B* **96**, 134510 (2017).

[21] J. Spałek, *Phys. Rev. Lett.* **59**, 728 (1987).

[22] M. Fidrysiak, J. Spałek, *Phys. Rev. B* **102**, 014505 (2020).

[23] M. Fidrysiak, J. Spałek, *Phys. Rev. B* **103**, 165111 (2021).

[24] M. Fidrysiak, J. Spałek, *Phys. Rev. B* **104**, L020510 (2021).

[25] M. Fidrysiak, D. Goc-Jago, J. Spałek, *J. Magn. Magn. Mater.* **539**, 168395 (2021).

[26] M. Fidrysiak, *Acta Phys. Pol. A* **143**, 180 (2023).

[27] J. Spałek, *Acta Phys. Pol. A* **111**, 409 (2007).

[28] J. Spałek, *Acta Phys. Pol. A* **121**, 764 (2012).